cm CHEMISTRY OF MATERIALS

Review

pubs.acs.org/cm

# Protocols for the Fabrication, Characterization, and Optimization of n-Type Thermoelectric Ceramic Oxides

R. Boston, W. L. Schmidt, G. D. Lewin, A. C. Iyasara, Z. Lu, H. Zhang,[†] D. C. Sinclair, and I. M. Reaney*

Functional Materials and Devices Group, Department of Materials Science and Engineering, University of Sheffield, Sheffield, United Kingdom S1 3JD

**ABSTRACT:** The development of oxides with high figure of merit, *ZT*, at modest temperatures (~300–500 °C) is desirable for ceramic-based thermoelectric generator technology. Although *ZT* is a compound metric with contributions from thermal conductivity ($\kappa$), Seebeck coefficient ($S$), and electrical conductivity ($\sigma$), it has been empirically demonstrated that the key to developing thermoelectric n-type oxides is to optimize $\sigma$ of the ceramic to ~1000 S/cm at the operating temperature. Titanate-based perovskites are a popular choice for the development of n-type oxide ceramics; however, the levels of $\sigma$ required cannot be achieved without control of the ceramic quality, significant reduction of the ceramic in low P($O_2$) atmosphere (e.g., $N_2$/5%$H_2$), and the use of specific dopants and dopant mechanisms, which allow the egress of oxygen homogeneously from the lattice. Here, we discuss the processing protocols to fabricate reliable, reproducible ceramic oxides and schemes for inducing high levels of $\sigma$, thereby optimizing the power factor (PF = $\sigma S^2$) and *ZT*. The problems associated with measuring $\kappa$, $\sigma$, and $S$ to achieve reproducible and accurate values of *ZT* are discussed, as are future directions which should enable further optimization. Finally, we comment on how these protocols may be applied to other systems and structures.

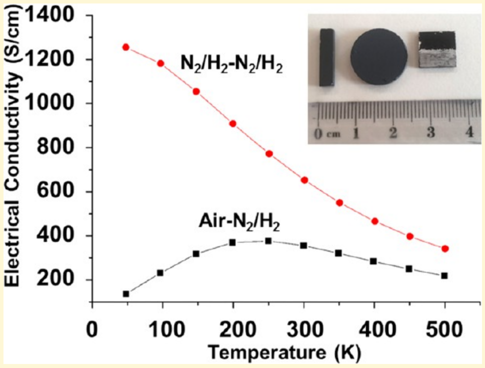

## 1. INTRODUCTION

Worldwide, many gigawatt hours of energy are wasted annually in the form of heat. Harnessing this waste heat is an opportunity to mitigate climate change and increase energy efficiency. World policies and regulations are set to move energy production from current technologies to renewable resources to reduce carbon emissions and curb the manmade impact on climate change. During this transitional period, the efficiency of current energy sources may be improved by the implementation of thermoelectric devices which turn waste heat into a useable form. In the Quadrennial Technology Review (QTR) 2015 by the US Department of Energy,[1] a survey of thermoelectric technology and its current potential can be found in Chapter 6G.[2] In summary, if thermoelectric generators with 2.5% conversion efficiency were to be implemented into manufacturing processes such as petroleum refining, chemical production, iron and steel, glass, etc., a total of 1880–4700 GWh/y could be recovered from the waste heat in these processes.[1] The range is from estimations of recovering 10 and 25% of the waste heat.[2] If we continue the analysis, according to the U.S. Energy Information Administration, the smallest generating capacity nuclear reactor could produce 11 496 MWh of power if run at full capacity for 24 h.[3] On a year-long run at full capacity, this would equal 4196 GWh/y. Power plants are seldom run at full capacity, and the numbers from the QTR 2015 place thermoelectric waste heat recovery in the range necessary to compete with even a small nuclear reactor. This possibility makes thermoelectric generators an attractive technology to increase the efficiency of current energy production and use. Thermoelectric generators (TEGs) contain no moving parts, as such require minimal maintenance, have long lifetimes, and produce no emissions,[4] and therefore represent a viable option for the recovery of waste energy.

The materials used in TEGs are judged by their figure of merit, *ZT*, as shown in eq 1, where $\sigma$ is the electrical conductivity, $S$ the Seebeck coefficient (sometimes referred to as thermopower), and $\kappa$ the total thermal conductivity.

$$ZT = \frac{S^2\sigma T}{\kappa} \tag{1}$$

As $\sigma$, $S$, and $\kappa$ are interrelated, it has proven difficult in some cases to find materials which are optimized for each parameter. $\sigma$ and $\kappa$, for example, are directly proportional to the carrier concentration, whereas $S$ has an inverse proportional relationship. Carrier mobility and other factors also contribute to each of these parameters, but their interrelationship(s) create significant challenges for materials scientists and engineers to find optimized compounds with reproducible $ZT > 1$.

**Special Issue:** Methods and Protocols in Materials Chemistry

**Received:** August 26, 2016
**Revised:** December 6, 2016
**Published:** December 7, 2016

DOI: 10.1021/acs.chemmater.6b03600
*Chem. Mater.* 2017, 29, 265–280

TEGs require the use of both n- and p-type conducting materials. Current devices are based around lead telluride and bismuth telluride compositions,[5] which, depending on doping, can be either n- or p-type.[4] These materials are an environmental concern, have a limited working temperature range,[6] and are prohibitively expensive to mass produce. They are reserved, therefore, for applications in which cost is not a primary consideration such as satellite propulsion and energy supply.[7] Although their working range is ∼200−600 K,[8] each material exhibits a temperature for $ZT$ maximum which can drop off dramatically within 20 K of the optimum.[8] The next generation of TEGs will need to consider earth abundance, toxicity, and thermal stability of the compositions to ensure they are viable for wide-scale industrial production.

Ceramic oxides exist in a wide range of crystal structures, encompassing most of the elements within the periodic table. Many ceramic oxides (including perovskite ($ABO_3$) and related crystal structure types such as Ruddlesden−Popper materials) exist in solid solutions due to chemical doping (cation and/or anion substitution) and/or via oxidation or reduction by processing under high or low oxygen partial pressure, $P_{O_2}$, respectively. This versatility can have a significant effect on the crystal structure and the electrical- and thermal-transport properties. Elements of a similar size with the same oxidation state as the host ions (i.e., isovalent dopants) are used to alter the unit cell size and crystal symmetry and lower the thermal conductivity but normally have limited influence on the electrical conductivity. In contrast, elements of similar size but different oxidation states (i.e., aliovalent dopants) and/or a change in $P_{O_2}$ during chemical processing can have a dramatic influence on the electrical properties (in addition to changes in crystal symmetry, unit cell size, and $\kappa$) and convert electrically insulating materials into semiconductors, metals, and even superconductors.[9] This ability to modify the chemical composition of oxides via chemical doping and/or appropriate processing under controlled $P_{O_2}$ conditions, along with their relative stability and low toxicity, makes them attractive materials for use in a wide variety of commercial functional devices.

With such a wide range of properties, it is unsurprising that ceramic materials can be fabricated which exhibit p- or n-type thermoelectric behavior. Some example compositions for both types of thermoelectric oxides, along with their $ZT$ values and associated temperatures, are listed in Table 1. This illustrates two important points about the field: first, good ($ZT > 1$) candidate p-type materials exist; however, there are no comparable n-types; second, the $ZT$ values are lower than those used in alloy-based TEGs. As a consequence, there is a current impetus to find novel compositions for n-type oxide materials with high $ZT$.

**Table 1. Selection of n- and p-Type Thermoelectric Oxides and the Corresponding ZT Values**

| compound | n/p type | $ZT$ | temperature for given $ZT$ (K) | ref |
|---|---|---|---|---|
| $Na_{0.89}CoO_2$ | p | 1.57 | 1100 | 10 |
| $Ca_3Co_{3.9}Fe_{0.1}O_9$ | p | 0.39 | 1000 | 11 |
| $Ba_{0.1}Ag_{0.1}Ca_{2.8}Co_4O_9$ | p | 0.29 | 973 | 12 |
| $La_{0.08}Sr_{0.92}TiO_3$ | n | 0.37 | 1045 | 13 |
| $La_{0.1}Sr_{0.83}Dy_{0.07}TiO_3$ | n | 0.36 | 1045 | 14 |
| $Ca_{0.9}Dy_{0.05}Yb_{0.05}MnO_3$ | n | 0.26 | 1000 | 15 |
| $La_{0.15}Sr_{0.775}TiO_{3-\delta}$ | n | 0.41 | 973 | 16 |

The data shown in Table 1 is a very small selection of the oxide materials interrogated for their thermoelectric properties. While there is still no accepted means to predict the thermoelectric properties of materials from their composition, there is now a critical mass of data which can be used for data mining, allowing for trends to be identified and exploited. Gaultois et al.[17] have successfully collated a wealth of data from the published literature, considering not only the material properties but also potential issues faced with supply and production of the scarcer elements using the Herfindahl−Hirschman Index which is used widely for commodities. They conclude by suggesting promising families of materials, including the early transition metal oxides, which show trends with high electrical conductivity. These materials may then be modified by using one of the methods to control thermal conductivity, potentially creating compositions with unprecedented $ZT$ values.[17]

One of the prominent n-type end member materials, as shown in Table 1, is strontium titanate, $SrTiO_3$, which is one of the many perovskite materials with an $ABO_3$ form. As an undoped material, $SrTiO_3$ has negligible thermoelectric properties, but these can be greatly improved by the addition or substitution of dopants and by processing under reducing conditions.[13−16] Most studies on rare-earth doping of reduced $SrTiO_{3-\delta}$ have used the direct substitution (or so-called donor (or electronic)-doping, i.e., $Sr_{Sr}^{x} \rightarrow La_{Sr}^{\bullet} + e'$) method which has resulted in modest improvements of $ZT$,[13−15] suggesting that this approach, though highly successful for other types of functionality, might not be the most efficient at producing optimized n-type thermoelectric oxides. An equivalent, but to-date more successful, route is to utilize dopants which create A-site vacancies in reduced $SrTiO_{3-\delta}$. One such study used La doping in reduced $SrTiO_3$ ceramics to create A-site vacancies by the partial substitution of $La^{3+}$ ions for the $Sr^{2+}$ ions in the ratio of 2:3 based on the general formula $Sr_{1-3x}RE_{2x}TiO_{3-\delta}$.[16] In these reduced materials, the A-site RE substitution, compensated by A-site vacancies, was also shown to increase solid solubility with respect to donor doping. Above 20 atom % doping, however, the compositions were found to be less stable in air and prone to reoxidation at modest temperatures, as shown by thermogravimetric analysis.[16] Despite these potential issues, A-site deficient $La_{0.15}Sr_{0.775}TiO_{3-\delta}$ to date has shown the highest $ZT$ (of 0.41 at 973 K) for a reduced n-type titanate-based perovskite ceramic.[16]

While the above schemes for the increase of carrier concentration are effective in giving an overall improvement in power factor ($PF = S^2\sigma$), they also act to increase the thermal conductivity, $\kappa$, which has the effect of reducing the value of $ZT$. Schemes to minimize $\kappa$ are based on the interruption of phonons, usually using some physical boundary, for example, through the inclusion of a large number of grain boundaries (i.e., nanoscaling of the microstructure). A grain boundary represents a potential scattering site to a phonon traveling through the lattice, meaning the mean free path and relaxation time between scattering events is reduced compared to that in the bulk crystal, reducing $\kappa$ within the material.[18]

Before any conclusions may be drawn on data reported about the properties of thermoelectric oxides, it is important to understand their synthesis. First, sample type must be carefully considered, i.e., does the data relate to single crystals, thin films, or bulk ceramics? Single crystals can give intrinsic properties, including that associated with any anisotropic response relating to specific crystallographic directions. Thin films are notoriously difficult to measure accurately, particularly $\kappa$, where the substrate plays a role, and for $S$ which requires a significant temperature gradient for accurate measurements. Bulk ceramics are most commonly measured, but our own in-house experiments demonstrate unambiguously that calcination and sintering temperature, drying starting reagents, and ceramic preparation can lead to dramatically different properties within a single composition.

Herein, we offer a set of experimental guidelines to assist in the preparation and study of n-type oxide thermoelectrics. We first address issues common to all oxide materials, namely, those associated with ceramic processing, and give examples of best practice for creating reliable and reproducible compositions. We examine the main challenges encountered in the chemical and structural characterization of thermoelectric oxides. Finally, we examine the means by which the three thermoelectric variables, $S$, $\kappa$, and $\sigma$, can be controlled, and outline procedures and pitfalls of measuring each, before the final calculation of $ZT$.

## 2. CERAMIC PROCESSING

The starting point for the synthesis of materials is always the choice of precursor. Traditional solid-state methods rely on suitable oxide and carbonate precursors, the majority of which are readily available and easy to obtain. "Straight-from-the-bottle" materials are, however, rarely in a form suitable for immediate use in solid-state processing, and care must be taken in preparing the starting reagents before synthesis. Since solid-state processing relies on precise stoichiometry and good homogeneity to ensure an even distribution of the different ions, it is prudent to measure the particle size and determine the composition of the raw materials; however, these simple steps are often overlooked in the early stages of processing, leading to irreproducible or unreliable results.

**2.1. Drying of Chemicals.** An inescapable aspect of materials chemistry is the presence of water and carbon dioxide which adsorb on the surfaces of any starting reagent and can lead to an appreciable increase in mass of the materials used. These additional molecules may seem insignificant as they will be lost in the later high temperature processing stages but must be removed before weighing or batching as this affects the stoichiometry of the reaction mixture. This becomes an important issue when aiming for well-defined product stoichiometry as any (nonintentional) nonstoichiometry will influence the final composition and can adversely influence properties such as the figure of merit, $ZT$. Straight-from-the-bottle $La_2O_3$ illustrates this point succinctly, and thermogravimetric analysis (TGA) shows a mass loss of 15% to 750 °C, Figure 1. The data were taken using a PerkinElmer Pyris 1 TGA with an alumina crucible and heated at 1 °C/min to 950 °C. The first mass loss between 290 and 360 °C is attributed to the loss of surface water, accounting for around 9% of the total mass. Between 460 and 520 °C a further 2% is lost as carbon dioxide desorbs from the surface. The final mass loss occurs over the range ~650 to 750 °C, at which temperature, 4% of the mass evolves which is attributed to the conversion of lanthanum hydroxide to lanthanum oxide. If $La_2O_3$ is left undried prior to the synthesis of $La_{0.1}Sr_{0.9}TiO_3$, the 15% discrepancy results in an actual stoichiometry of $La_{0.085}Sr_{0.9}TiO_{2.987}$ or potentially a mixture of phases.

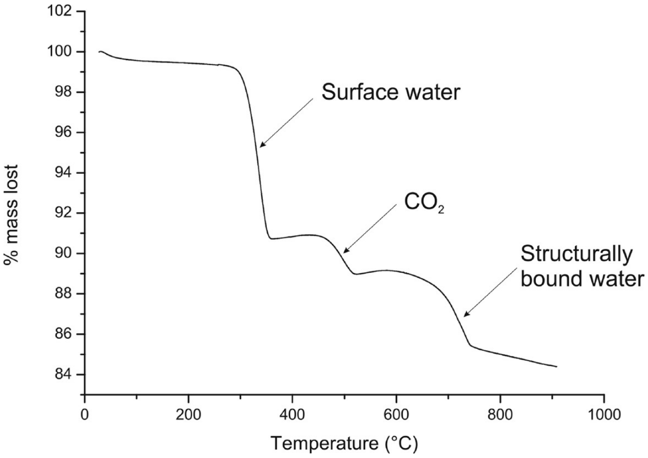

**Figure 1.** Heating cycle thermogravimetric analysis of "straight-from-the-bottle" $La_2O_3$ showing a 15% loss of the total mass.

This data also illustrates it is inadequate to dry materials at just above the boiling point of water, as bound water is often not completely lost until much higher temperatures, along with adsorbed $CO_2$. The precise temperature to fully dry materials should therefore be determined on a material-by-material basis using a combination of TGA and XRD, and hot dried precursors should be stored in a desiccator until cooled to room temperature and batched immediately to avoid significant readsorption of $H_2O$ or $CO_2$. Furthermore, such data can be useful in identifying volatile elements, allowing predictions about the proportion of a reagent that may be lost during calcination. Some oxides are well-known to have variable or mixed oxidation states, but this does not necessarily create a problem, providing the dried starting powder is of known composition and the phase has been checked by XRD. For example, although many Mn-containing oxides can contain mixed valence states (eg $Mn^{2+}/Mn^{3+}$ or $Mn^{3+}/Mn^{4+}$) in the final sintered ceramics, they can usually be prepared via a variety of commonly used Mn-based precursors of either fixed valence, including $MnCO_3$ ($Mn^{2+}$), $Mn_2O_3$ ($Mn^{3+}$), or $MnO_2$ ($Mn^{4+}$), or by mixed valence, e.g., $Mn_3O_4$ ($Mn^{2+}$ and $2Mn^{3+}$). The valence state(s) of the Mn ions in the final sintered ceramic readily adjust to the $T/P_{O_2}$ conditions used during ceramic processing.

When using nonoxide or carbonate materials (nitrates, acetates, hydroxides, etc.), full knowledge of the composition becomes especially important, particularly as their generally low melting/decomposition temperatures make them unsuitable for high-temperature drying. Many of these classes of materials are also hygroscopic and/or have high numbers of waters of crystallization, for example, strontium hydroxide octahydrate. This number can vary considerably depending on the age of the chemical, storage conditions, and even the time of year. As such it is important to determine the exact water content of each material using TGA, so as to accurately account for variations in mass when batching.

M. Li et al.[19] have demonstrated the importance of drying through the synthesis of the titanate-based perovskite $Na_{0.5}Bi_{0.5}TiO_3$, NBT. Although NBT is not a thermoelectric material, the electrical properties are highly dependent on very small variations in the Na/Bi ratio, illustrating the need for drying. In particular, if the Na/Bi starting stoichiometry ratio is $\geq 1$, then it is an excellent oxide-ion conductor, whereas if Na/

Bi < 1 then it is a dielectric (electronic insulator). The precursor $Na_2CO_3$ is hygroscopic, and if not dried prior to batching it has the formula $Na_2CO_3 \cdot nH_2O$ where $n$ is typically ~0.05 to 0.1 with the precise value of $n$ dependent on the source powder but which may be readily established by TGA. A batch of stoichiometric $Na_{1/2}Bi_{1/2}TiO_3$ prepared from dried $Na_2CO_3$ with Na/Bi = 1 has high oxide-ion conductivity, whereas an attempted stoichiometric batch prepared from the reagent straight from the bottle ($Na_2CO_3 \cdot 0.06H_2O$) corresponds to a composition of $Na_{0.495}Bi_{0.50}TiO_{2.9975}$ and therefore Na/Bi < 1, which is an excellent dielectric with very low bulk conductivity with a high activation energy, $E_a$, for conduction, Figure 2. NBT highlights the dramatic impact that a very small level of unintended nonstoichiometry, e.g. −0.005 mol % Na associated with a "wet" reagent powder, can have on the electrical properties of a titanate-based perovskite.

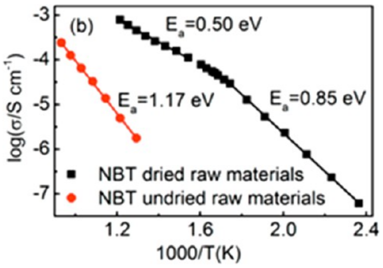

**Figure 2.** Arrhenius plots of bulk conductivity for $Na_{0.5}Bi_{0.5}TiO_3$ ceramics prepared using "straight-from-the-bottle" ($Na_2CO_3 \cdot 0.06H_2O$) and predried ($Na_2CO_3$) reagents. Reproduced with permission from ref 19. Copyright 2015 American Chemical Society.

While NBT is a special case, with a highly complex domain and microstructure, it highlights the sensitivity of electrical properties to composition. In materials where control of the electrical and thermal transport properties is paramount, such as thermoelectrics, this aspect of processing must not be ignored.

To illustrate the effect of drying on a thermoelectric oxide, samples of $SrTiO_3$ were synthesized using precursors straight from the bottle without any predrying (following all of the other solid-state procedures as usual). The X-ray diffraction (XRD) data of the undried is superficially identical to correctly prepared $SrTiO_3$; however, calculation of the lattice parameters reveals the size of the unit cell is slightly smaller compared to that normally quoted: 3.901 ± 0.002 Å as opposed to the expected 3.905 Å,[20] suggesting nonstoichiometry.

**2.2. Particle Size.** Solid-state processing is entirely reliant on diffusion of ions to form a homogeneous final product. While some ions are highly mobile and can rapidly reach homogeneity during calcination, many multielement materials are prone to forming core−shell structures, dictated by limited cation diffusion rates, such as in doped $BaTiO_3$.[21] To minimize synthesis time, it is desirable to have a small particle size before calcination. Mechanical milling of materials is one of the most reliable methods for controlling precursor particle size. Standard ball milling using yttria-stabilized zirconia (YSZ) media (Figure 3a) is commonly used to reduce the size of starting powders. If milling is performed after batching it is an easy way to thoroughly mix and evenly distribute precursor materials. Attrition milling using smaller YSZ media (Figure 3b) offers a rapid and more high-energy method for mixing and reduction in particle size; however, there is the possibility of introducing impurity elements from the milling media into the reaction, either from the media itself or from improper cleaning prior to reuse, as can be seen in Figure 3b. Bäurer et al.[22] showed, for example, that ball milling of strontium titanate using YSZ media could introduce 0.064 wt % contamination (mainly as $Zr^{4+}$),[22] well above detection limits of, e.g., inductively coupled plasma-optical emission spectroscopy.

Another traditional method for the grinding and homogenization of precursors is to use a mortar and pestle and grind the materials by hand. This is not recommended for reproducible materials for a number of reasons. First, the process is likely to produce crystallites with inconsistent sizes, which is detrimental to the solid-state reaction process. The degree of mixing will be lower in mortar and pestle-prepared samples, again to the detriment of the solid state process. The mortar and pestle can also introduce a significant level of contamination, especially if the powders being ground are harder than the mortar and pestle material. In the case of agate-

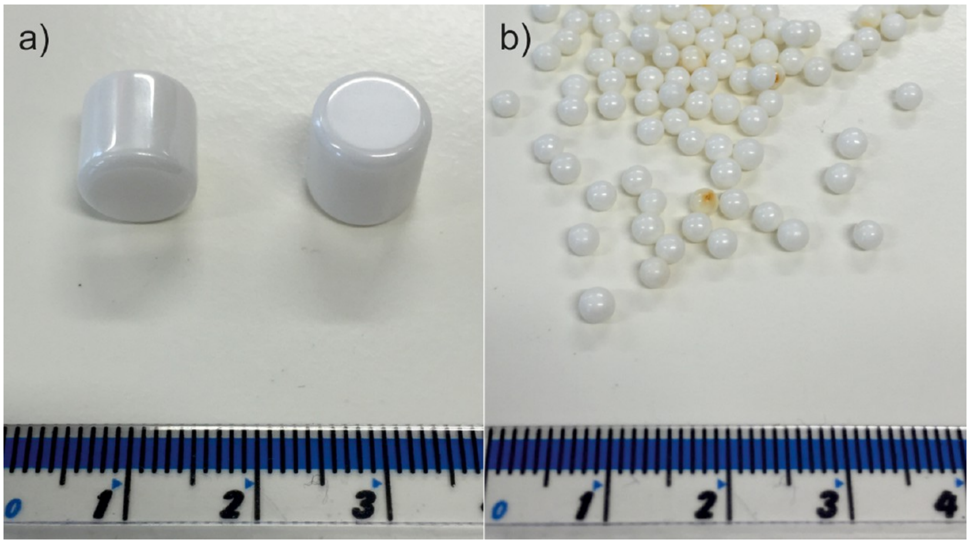

**Figure 3.** Two typical types of yttria-stabilized zirconia milling media: (a) 1 cm mill media and (b) 2.5 mm bead attrition mill media. One of the beads is discolored and therefore contaminated.

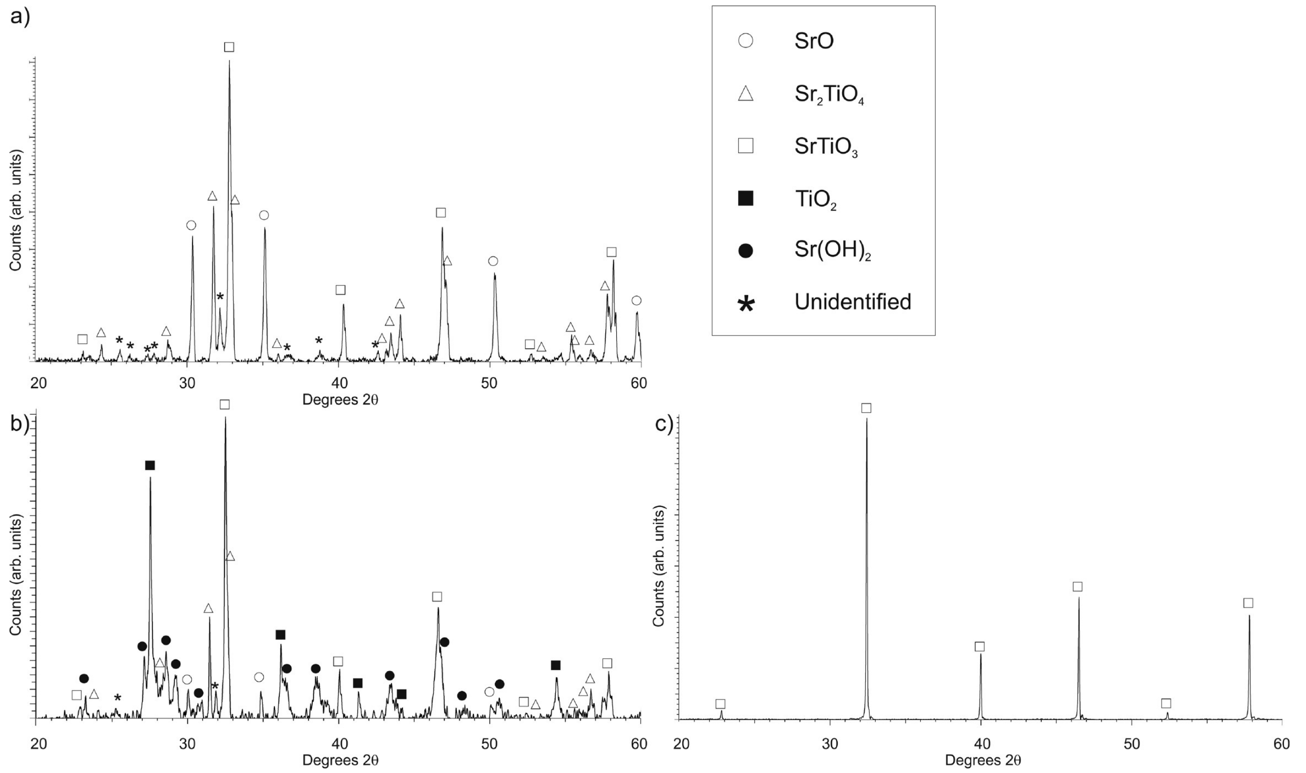

**Figure 4.** X-ray diffractograms of (a) as-prepared $SrTiO_3$ synthesized without milling, "$SrTiO_3$-unmilled", (b) the same sample having been mechanically milled after calcination, and (c) $SrTiO_3$ prepared with milling of the starting materials before calcination, "$SrTiO_3$-milled".

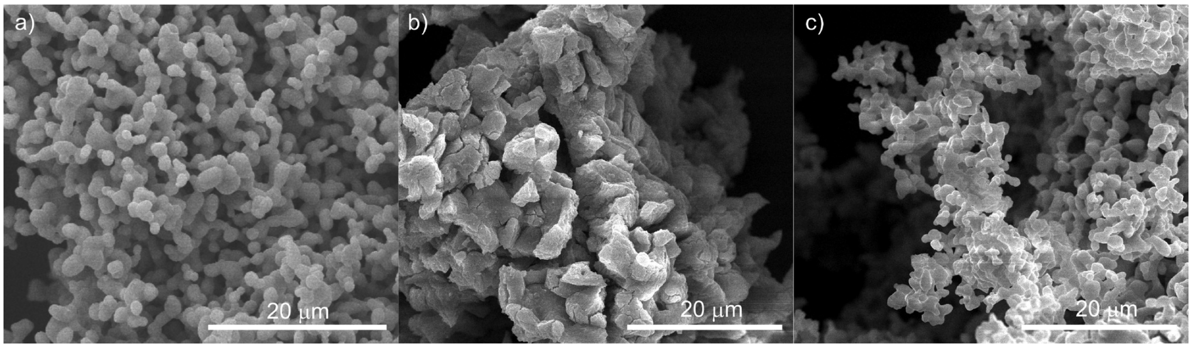

**Figure 5.** SEM micrographs of (a) $SrTiO_3$-milled which has been milled prior to calcination; (b) and (c) illustrate the variation in morphology across a single sample of $SrTiO_3$-unmilled.

based mortar and pestles, contamination can take the form of silica which is a well-known sintering aid.[23] This can have multiple complex effects on the system, including the formation of intermediate phases or the introduction of a liquid phase.[23] While this might be superficially advantageous, this can lead to inaccurate or unreproducible compositions. Finally, mortar and pestle grinding is generally limited to small batch sizes. This is one of the key advantages of ball milling: samples on 100 g scale in the laboratory (100 kg scale commercially) can be reliably produced with only a fraction of the effort and hands-on time of a sample prepared using a mortar and pestle.

To illustrate the need to mill materials, samples of $SrTiO_3$ were synthesized with and without milling of the precursor materials. The ball-milled sample (hereafter called $SrTiO_3$-milled) was milled using YSZ media (Figure 3a) in isopropanol for 16 h prior to calcination, and a second sample was synthesized from dried but unmilled precursors (hereafter called $SrTiO_3$-unmilled), with the two precursors being stirred by hand before calcination. $SrTiO_3$-unmilled is composed of some $SrTiO_3$ and significant quantities of SrO, strontium-rich tetragonal $Sr_2TiO_4$, and some minor unidentified phases. Calculation of the lattice parameters showed the $SrTiO_3$ formed did not have the expected unit cell dimensions, with an $a$ parameter of 3.867 ± 0.016 Å (as opposed to the expected 3.905 Å).[20] In contrast, $a$ for the $SrTiO_3$-milled sample was 3.903 ± 0.002 Å, in accordance with the expected value.[20]

Post calcination milling substantially changes the composition of the $SrTiO_3$-unmilled sample. The majority of the SrO phase is converted to $Sr(OH)_2$ by the isopropanol, observed as a reduction in the relative peak height of the SrO phase and the appearance of additional peaks. Post calcination ball milling also reveals the presence of large quantities of unreacted $TiO_2$ which were previously masked inside a coating of $SrTiO_3$. Upon ball milling, the large heterogeneous agglomerates are broken apart to reveal the unreacted starting materials inside as shown in Figure 4b. This indicates the likely formation mechanism of

$SrTiO_3$, with the more-mobile strontium ions diffusing into the titanium phase during calcination. This mechanism is supported by the presence of the strontium-rich $Sr_2TiO_4$ phase which forms as an intermediate and highlights the importance of milling steps before and after calcination. Prior to calcining, the materials must be given the highest possible surface area to maximize the number of reaction sites. Equally, post calcination milling before XRD is key to identifying possible unreacted materials which would otherwise be missed.

Scanning electron microscopy (SEM) reveals the differences in morphology of the final product. SEM micrographs of as-prepared $SrTiO_3$-unmilled and $SrTiO_3$-milled are shown in Figure 5. The morphology of the $SrTiO_3$-milled sample particles (Figure 5a) have a regular, smooth appearance, whereas the $SrTiO_3$-unmilled sample shows variation across the crystallites. Some regions of regular, smooth crystallites were observed and attributed to the reacted $SrTiO_3$ phase (Figure 5c). In addition to these morphologies, other, more irregular regions were observed (Figure 5b), likely to be the unreacted/partially reacted materials. Proper prepreparation is therefore key to achieving homogeneity in both phase and morphology.

**2.3. Cross-Contamination.** The furnace used to calcine and sinter ceramics represents an opportunity for the introduction of contaminants. Many elements are volatile at the high temperatures used during processing, and as such can easily be lost from reaction mixtures leading to a non-stoichiometric product. Some volatiles are lost through the chimney or gas outlet, but the majority are absorbed by the furnace lining. These materials can be redeposited onto subsequent samples leading to surface layer contamination, as shown in Figure 6. Careful control of furnaces and their elements is therefore important, especially for perovskite materials whose wide compositional tolerances permit a range of A- and B-site substitutions which have little effect on crystal structure but which have a greater (and often detrimental) effect on electrical properties.[24] It may be prudent, therefore, to regulate or limit the elements which can be used in each furnace, thus reducing the likelihood of accidental cross-contamination. Another means to reduce cross contamination (and in some cases volatilization) is to use a crucible with a lid. This not only helps to prevent cross-contamination, but by marginally increasing the vapor pressure of the volatile elements within the crucible, can actively prevent elemental loss.

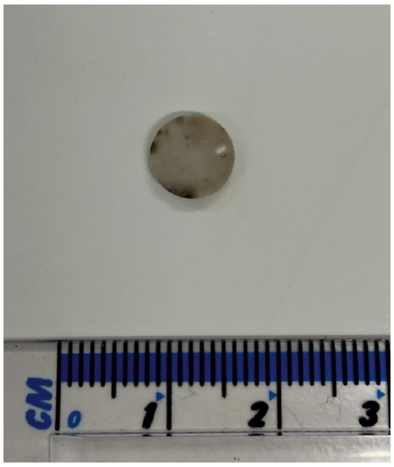

**Figure 6.** Contaminated sintered ceramic showing at least two different local contaminants observed as a change in color.

**2.4. Pellet Preparation.** In many cases to generate reproducible data, reliable sintered ceramics must be produced. There are many methods to consolidate powders; we will cover uniaxial pressing and cold isostatic pressing here as two examples of simple and routinely performed lab-based consolidation techniques. Uniaxial pressing consists of loading finely grained calcined powder (which may need to be milled after calcination to achieve this) into a die (often cylindrical or oblong) and applying pressure along one axis using a hydraulic press. Attainable applied masses vary by manufacturer and model, but up to 25 tons is easily achievable. This can then be converted into a pressure depending on the size of die used. Hold time at pressure and applied load must be tailored to each material, but generally the green densities produced are ~50–60%. Cold isostatic pressing uses hydraulic fluid to exert a pressure in every direction on the green body, which must be produced in a uniaxial press first. To prevent mixing of the fluid with the powder, samples are generally placed inside a flexible receptacle, for example, a nitrile laboratory glove. Air needs to be removed using a vacuum pump, as, at the pressures produced, it would cause the glove to fail. Again achievable pressures vary by make and model, but ~30 kPa is routinely available. In both of these techniques, the applied pressure must be tested for each material; too low and the green body will be mechanically too weak to remove as a single piece from the die or receptacle, and too high results in pressing faults such as capping in the body.[25] In the case of rare earth doped $SrTiO_3$ compositions discussed within this article, green bodies were prepared by using 1 ton uniaxial hydraulic pressing for 1 min followed by cold isostatic pressing at 200 MPa for 1 min. Other consolidation techniques, covered elsewhere, include hot isostatic pressing[26] and the emergent cold sintering processes.[27]

Once pressed, test samples are heated to a temperature that is usually 100–200 °C higher than the calcination temperature to promote densification. Volatilization of elements can present a particular issue here with the higher temperatures used, and the choice of crucible may also become a consideration. Some materials will react with, leach into, or fuse with alumina, particularly at higher temperatures. This can be prevented through the use of different crucible materials such as platinum; however, cost is often prohibitive. One lower cost solution is to use a piece of platinum foil as a cover for the base of the crucible, which will prevent any reaction or sticking, but has the advantage of being cleanable and reusable, and if the sample is accidentally melted, is less of a loss. Another way to achieve this is to create a small pile of calcined powder and seat the green ceramic on this; however, this may still lead to reaction with the alumina, making the crucibles single-use. Pellets produced using this method also require considerable polishing to remove adhered powder, and this makes the uniformity of the ceramic more difficult achieve.

In spite of the possibility of nonuniformity, it is often advantageous to remove the surface layers of sintered ceramics, as this offers the opportunity to reduce the likelihood of chemical contamination from the sintering process and can be achieved simply by using grinding paper, such as silicon carbide or diamond. This can be performed by hand or using a mechanical polisher. Care must be taken, however, as the process can easily introduce inconsistencies in thickness, especially when grinding by hand.

Upon completion of this process, the density of the sintered body must be determined. There are two common ways to do this, either by taking the dimensions (volume = area × thickness) and mass or by using an Archimedes density balance which uses the buoyancy and mass. There are pros and cons for both methods: the direct measurement method relies on a sintered body with uniform geometry for accurate dimensions. In the case of disks where the radius is squared to obtain the area, any errors here are rapidly propagated into the final volume value, and the Archimedes method is unable to cope with highly porous samples.

Once the density has been calculated, it is helpful to put the value found into context by calculating the theoretical maximum density. This is trivial for well-known materials as values can be found in the literature. For novel compositions, however, this density maximum must be found by other means. This can be achieved by finding the unit cell volume from XRD using eq 2, which links the density ($\rho_{\max}$) with the molar mass ($A$), unit cell volume ($V_c$), number of formula units per unit cell ($N_c$), and Avogadro's number ($N_A$).

$$\rho_{\max} = \frac{N_c A}{V_c N_A} \qquad (2)$$

A high density is vital for accurate and reproducible data, especially when screening large numbers of novel single-phase materials (composites are beyond the scope of the discussion here). Ceramics to be used for characterization should be single phase and preferably have a density >95% of the theoretical maximum, keeping porosity to a minimum. Sintering aids can be added[23] during the formation of the green body and prior to sintering but must be considered on a material-by-material basis, and care must be taken to understand fully their action and any possible impact they may have on the system (for example, the formation of secondary phases). This consistency is important for the interpretation of data and also for mechanical stability, which is required for techniques such as the measurement of $\sigma$ and $S$, which often use spring contacts which apply forces across the ceramics. Assuming a ceramic is of sufficiently high density, as discussed above, it can then be prepared for testing. Figure 7 shows the pellets prepared for measurements on a Netzsch SBA 458 Nemesis (left bar) and an Anter Flashline 3000 (right square). The 10 × 10 mm square has been cut from the disk, leaving edge pieces which can be made available for microstructure analysis. The bar and square are polished into the proper dimensions for each instrument. One must know the requirements for the available instrumentation. It is possible to sinter a large enough pellet and cut the required shapes necessary for measurement; however, the instrumentation and processing facilities may limit this option requiring separate pellets to be prepared for each system.

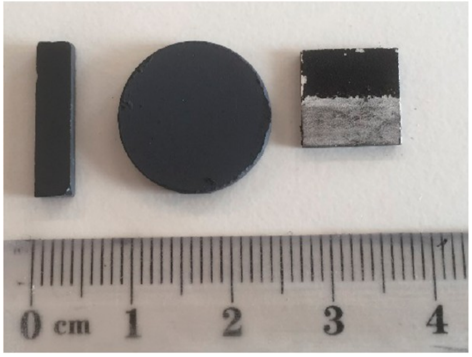

**Figure 7.** From left to right, a sintered bar prepared for $\sigma$ and $S$ measurement on the Netzsch SBA458 Nemesis system and a 20 mm disk (~16 mm after sintering) which is then cut into a 10 × 10 mm square for analysis on the Anter Flashline 3000. The square is coated with a silver electrode paste (visualized on the bottom half), and the top has the graphite coating which is required for $\kappa$ measurements.

Once synthesized and processed, the next step is to characterize fully the structure and chemical composition of samples at both a macroscopic and a local level. This is important not only to ensure the material is free of secondary phases but also to gain knowledge of the local chemistry and structure. This is key to interpretation of the electrical and thermal properties.

## 3. INTERPRETATION OF STRUCTURE

The main issue with interpreting structure of thermoelectric oxides is the absence of high quality structural data from standard instrumentation. In-house XRD, for example, gives only cursory information about the structure and is used primarily to give an indication of solid solubility of dopants and the presence of secondary phases above a few vol %. A sequence of XRD traces of a $Sr_{1-3x/2}La_xTiO_{3-\delta}$ solid solution sintered in $N_2$/5% $H_2$ is shown in Figure 8. For a full interpretation of the data the reader is referred to Lu et al.[16] The appearance of specific peaks (denoted by *) as a function of composition implies the onset of cell doubling phase transitions relating to octahedral rotations. Additionally, the absence of a secondary phase suggests there is a full solid solution between $La_{2/3}TiO_3$ and $SrTiO_3$ when sintered in $N_2$/5% $H_2$. This XRD data, however, gives only limited information concerning critical structural aspects of the solid solution. Crystal chemistry criteria based on the perovskite tolerance factor and the symmetry of the end members suggest that at some value of $x$ the untilted $SrTiO_3$ distorts by rotations of O-octahedra in antiphase, followed by an in-phase O octahedral tilt transition.[28] The sensitivity of XRD to distortions of O

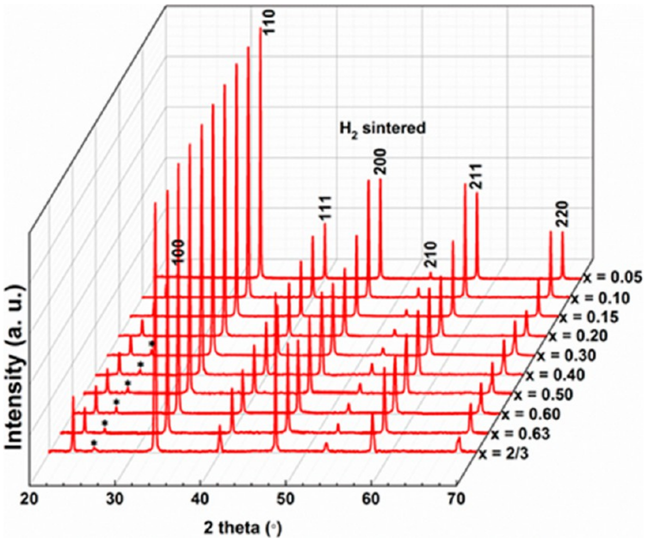

**Figure 8.** XRD traces from $Sr_{1-3x/2}La_xTiO_{3-\delta}$ as a function of $x$ in compositions sintered in $N_2$/5% $H_2$. Reproduced with permission from ref 16. Copyright 2016 American Chemical Society.

octahedra is notoriously poor.[28] Neutrons are more sensitive to O, but obtaining such diffraction data requires the use of national facilities. Instead, we encourage the use of electron diffraction and transmission electron microscopy to study the onset of O octahedral tilt transitions and to study local structure arising from clusters of A-site vacancies ($V_A$). ⟨110⟩ zone axis electron diffraction patterns from $x = 0.3$ and 0.5 are shown in Figure 9, illustrating that the former composition is tilted in antiphase (a reflections) while the latter is tilted in phase and in antiphase with a contribution to some of the superstructure reflections from ordered $V_A$ (M reflections). For an understanding of the planar defects relating to phase transitions and ordering, two beam dark field imaging is a powerful tool, especially if coupled with aberration corrected TEM. The planar defects for air-sintered $Sr_{1-3x/2}La_xTiO_3$ with $x = 0.5$ obtained with an antiphase tilt refection are shown in Figure 10a. Weak ferroelastic domains are observed interlaced with antiphase boundaries. For identification of $V_A$ clusters, the Rutherford scattering associated with aberration corrected TEM gives Z contrast high resolution images in annular bright and dark field mode. $V_A$ clusters can be readily identified, as illustrated in Figure 10b.

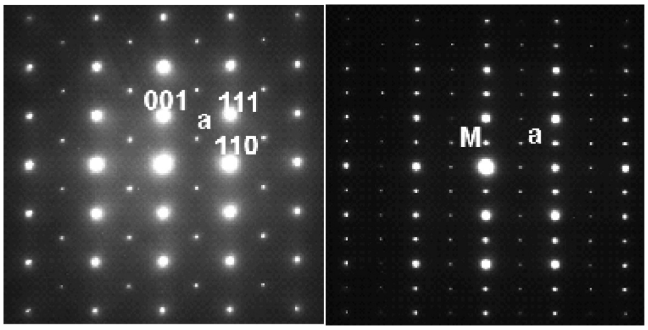

**Figure 9.** ⟨110⟩ zone axis diffraction patterns from $Sr_{1-3x/2}La_xTiO_{3-\delta}$ showing the sensitivity of electron diffraction to the onset of O-octahedra tilt transitions. a = reflections in antiphase, and M indicates mixed reflection relating to in-phase tilting and $V_A$ ordering. Reproduced with permission from ref 16. Copyright 2016 American Chemical Society.

## 4. CONTROL AND MEASUREMENT OF THE THERMOELECTRIC PROPERTIES; κ, S, AND σ

The three variables which make up the thermoelectric figure of merit, *ZT*, have a complex relationship and so cannot be considered as separate entities when devising schemes to maximize *ZT*. The electrical conductivity ($\sigma$) and Seebeck ($S$) coefficient have the most explicit interdependence, which can be clearly seen from their respective equations. In simple terms, $\sigma$ is dependent on the number of charge carriers ($n$), the carrier mobility ($\mu$), and the carrier charge ($e$), as described by eq 3.

$$\sigma = n\mu e \tag{3}$$

Here, it is obvious that an increase in the carrier concentration will increase $\sigma$. This is detrimental to the magnitude of the $S$, however, which is proportional to $n^{-2/3}$, as shown in eq 4, which is valid for metals and degenerate semiconductors[29] where $k_B$ is the Boltzmann constant, $e$ is the elementary charge, $h$ is the Planck constant, $m^*$ is the effective mass of the carrier, and $T$ is the temperature.

$$S = \frac{8\pi^2 k_B{}^2}{2eh^2} m^* T \left(\frac{\pi}{3n}\right)^{2/3} \tag{4}$$

This complex interplay means there is no one ideal solution to improve *ZT*. The thermal conductivity, $\kappa$, is defined in eq 5 as the addition of phononic ($\kappa_L$) and electronic ($\kappa_E$) contributions.

$$\kappa_{\mathrm{total}} = \kappa_L + \kappa_E \tag{5}$$

The Wiedemann–Franz law describes how the carrier concentration affects the electronic contributions; $\kappa_E = ne\mu LT$ where L is the Lorenz number. In simpler terms, however, the more carriers there are, the more carriers are available to transmit heat within the lattice and therefore to increase $\kappa_{\mathrm{total}}$. This shows now that all three variables for the determination of ZT are dependent on the carrier concentration. If the thermal conductivity is to be reduced, the lattice contributions, $\kappa_L$, become an important variable to control, without being detrimental to $S$ or $\sigma$.

In this section each of the three variables is considered in turn with emphasis on some schemes for their relative optimization and to examine some common methods for their measurement. The information is presented to complement previous comprehensive reports covering thermoelectric property measurement techniques which include suggested protocols based on worldwide round-robin experiments[30,31] and a more recent review of the errors associated with each measurement technique.[32]

**4.1. Control and Measurement of Thermal Conductivity.** Of all the controllable properties of thermoelectric materials, one of the most challenging is $\kappa$, which must be minimized for high *ZT*. $\kappa$ is often closely linked to $\sigma$, with both properties being controlled/dominated by the motion of

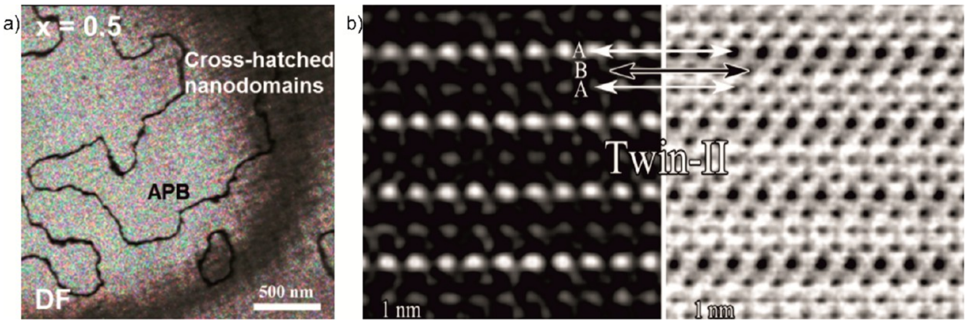

**Figure 10.** (a) Two beam dark field superlattice reflection obtained using an antiphase tilt reflection and (b) annular dark and bright field images of a $V_A$ cluster. Reproduced with permission ref 16. Copyright 2016 American Chemical Society.

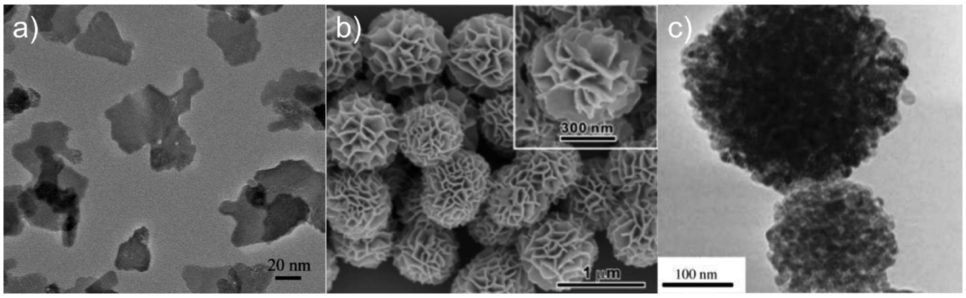

**Figure 11.** Examples of hydrothermally grown $SrTiO_3$ crystallites. (a) Nanosheets grown using ethylene glycol (reproduced with permission from ref 42), (b) self-assembled nanoflowers (reproduced with permission from ref 43), and (c) nanospheres (reproduced with permission from ref 44). Copyright 2013 Royal Society of Chemistry (a, c) and American Chemical Society (b).

electrons within the lattice. Correspondingly, schemes to improve $\sigma$ often result in an observed increase in $\kappa$, which is then detrimental to $ZT$. As such, other, nonelectronic means of controlling $\kappa$ are employed. Of these, ionic radius (and mass) of chemical dopants[33] and ceramic microstructure[34,35] are the two best-documented methods. In both cases, the aim is to disrupt the progress of phonons through the lattice, either through scattering from ions or vacancies within the lattice which cause local deviations from the regular crystal structure, or through the incorporation of a large number of grain boundaries (i.e., nanostructuring or specific control of crystallite morphology). The grain boundaries act as scattering sites for the phonons, increasing the likelihood of a scattering event and reducing the transfer of heat through the bulk.[18] The chemical means to control $\kappa$ are covered in detail elsewhere,[36] so in this section we examine the micro- and nano-structuring approach as a means of reducing $\kappa$.

Control of the microstructure of the final ceramic is a well-known method of influencing $\kappa$.[34,35,37] This relies on the creation of crystallite morphologies in the calcined powders which are retained throughout the sintering process, creating, for example, microstructures which have large numbers of grain boundaries. There are numerous pathways to control these crystallite morphologies in oxide materials. Hydrothermal techniques are perhaps the best known, relying on high pressures to drive the formation of oxides from solution over a period of hours to days.[38,39] There have been several attempts to create hydrothermal powders of thermoelectric materials; the majority of these have been p-type materials.[38−40] However, n-type RE-doped $SrTiO_3$ has been synthesized as nanoscale cubes using hydrothermal methods and showed an increase in Seebeck coefficient (due to electron filtering effects and constraining of the band structure)[41] over the equivalent bulk solid state powders, while simultaneously producing a reduction in $\kappa$.[32] Other morphologies are possible such as nanosheets,[42] flowers,[43] and nanospheres synthesized,[44] as shown in Figure 11. Effective though these methods are for the control of powder crystal morphology, there have been few attempts to incorporate them into testable thermoelectric ceramics.

A comprehensive report on the control of microstructure to influence thermal properties was performed by Buscaglia et al.[35] in which the microstructure of the sintered ceramic was controlled by using starting materials of a specified size. By limiting the size of the crystals in the starting materials, they demonstrated $\kappa$ could be reduced by an order of magnitude over the single crystal equivalent in La-$SrTiO_3$.[35] They also concluded, however, that nanostructuring adversely affected $\sigma$ (due to the low sintering temperatures used to preserve the nanostructures). This may be remedied, however, with rapid or low temperature sintering techniques such as spark plasma sintering.[45,46]

Laser Flash systems are the most common way to determine $\kappa$ of a bulk ceramic sample. In most cases, Laser Flash systems work by applying a burst of energy to one side of a sintered ceramic sample, with the heat energy transmitted through the sample detected in the infrared. Samples should be prepared to the ASTM E1461-13/E2585 standard[47] for $\kappa$ measurements. As stated in the standard, sample surface is important, and it is normal for pellets to require first a layer of silver or gold to increase the opacity of the sample, e.g., by painting on electrode paste, or sputtering, followed by a layer of graphite to reduce the reflectivity of the surface. This layer is generally applied from a spray can, and a spray station can be set up using an empty box to contain extraneous spray. The graphite coating should be evenly applied across the surface, with enough applied to form a full covering but without excess thickness. For $\kappa$ to be calculated, the three variables in eq 6 must be obtained: thermal diffusivity ($\alpha$) is calculated directly from the data generated by the laser flash system, density ($\rho$), and specific heat $C_p$.

$$\kappa = \alpha C_p \rho \tag{6}$$

Density can be determined by using the geometric dimensions and mass, Archimedes method, or dilatometry. Each technique offers an uncertainty that is carried through the calculation of $\kappa$. Borup et al.[32] has discussed in detail the first two density methods. They indicate that the variation in thickness should be less than 0.005 mm to reduce geometric errors and the Archimedes principle can overestimate the density when samples are porous and absorb the liquid. They have offered advice to check the absorption by measuring the sample in air again to determine if any liquid is present, which allows the experimentalist to determine whether this is a viable method for density determination of samples. While the density is often assumed to be temperature independent,[32] dilatometry can be used to determine whether the dimensions of a material change at temperature. Although this is an isotropic measurement, anisotropic thermal expansion can have further detrimental effects on the properties if they are not measured along the same direction.[32]

The specific heat, $C_p$, of a material can be determined in some commercial laser flash systems when measured alongside a reference material according to eq 7. This method of determining $C_p$ can be inaccurate leading to an underestimation of $\kappa$.[32] Methods for measuring $C_p$ of a material include drop calorimetry, differential scanning calorimetry (DSC), or heat flow methods such as using a Quantum Design physical property measurement system (PPMS). DSC is now a common method used in academic laboratories, and a round-robin study by Wang et al.[31] has shown that up to 15% discrepancy in $C_p$ data can occur between laboratories, decreasing to approximately 5% when standard methods such as the ASTM standard E1296 are explicitly followed.[31] Borup et al.[32] have also discussed the errors and uncertainties associated with the determination of $C_p$, and all parties agree that measured values should always be compared to that calculated from the Dulong-Petit law.[32] In two reports Leitner et al.[48] have also described in detail the Neumann-Kopp estimation of $C_p$ values for materials with no reported literature values.[49] As these are calculated by combining the values from known binary oxides, care must be taken as these are estimations and can deviate from realistic values due to nonstoichiometry (for example, oxygen deficiency)[48] in the final compound.[48] The reader is directed to the references used in this section for more in-depth coverage of the complexities of estimating and measuring $C_p$, and we concur that discussion of this data is often lacking in reports for thermoelectric materials. To understand the uncertainty and accuracy of reported thermal conductivities, $C_p$ data must be thoroughly discussed.

$$C_p = \frac{(mc\Delta T)_{\text{reference}}}{(m\Delta T)_{\text{sample}}} \tag{7}$$

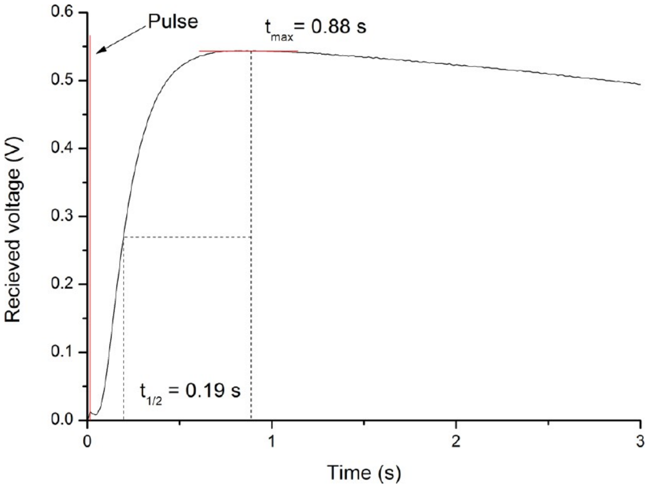

**Figure 12.** Example of typical data obtained from the Anter Flashline for a sample of $Pr_{0.4}Sr_{0.4}TiO_{3-\delta}$. The value for $t_{1/2}$ is 0.19 s, well within the 0.3 s required to minimize conductive losses through the sample holder.

An example of data collected using the laser flash method is shown in Figure 12. The data were taken on an Anter Flashline TM 3000, which utilizes a high-speed xenon discharge flash, and has a variety of different reference sources, some of which are made in-house. In this case a thermographite reference standard was used for the instrument to estimate the $C_p$ values to determine $\kappa$. The initial pulse is shown at $t = 0.016$ s, with the transmitted energy increasing to a maximum at $t = 0.88$ s before decaying. The most important point to note when preparing samples for the laser flash system is that they must be thin enough for the value of $t_{1/2}$ (the time taken for the sample to initially reach half of the eventual plateau value) to be ≤0.3 s. This is important to minimize other heat losses through conduction through the sample holder or convection with the surrounding air. This depends heavily on the sample and may be moderated using thickness. Samples with low values of $\kappa$ must be carefully thinned to meet this requirement, while retaining uniformity in thickness.

There are several methods for the extraction of $\alpha$ from the flash line plot. The simplest of these is the Parker method[50] and will give a good approximation for $\alpha$ using the relationship given in eq 8, where $L$ is the thickness of the sample.

$$\alpha = \frac{0.1388L^2}{t_{1/2}} \tag{8}$$

This is limited, however, as it takes no account of heat losses and assumes an instantaneous pulse. There have been numerous modifications to this interpretation, including the Cowan method[51] which uses the cooling section of the pulse, the Heckman method[52] which considers the impact of a noninstantaneous pulse, and the Clark and Taylor method,[53] which is widely used. Rather than being a single equation, the Clark and Taylor method compares different ratios on the heat-loss curves for the material with the adiabatic case, and assumes that the deviations between the two relate to heat losses (i.e., the nonadiabaticity of the system). This is generally done internally by the thermal conductivity instrument and gives a good error correction for the conductive and convective heating losses during the experiment, thus giving a more accurate value for $\alpha$.

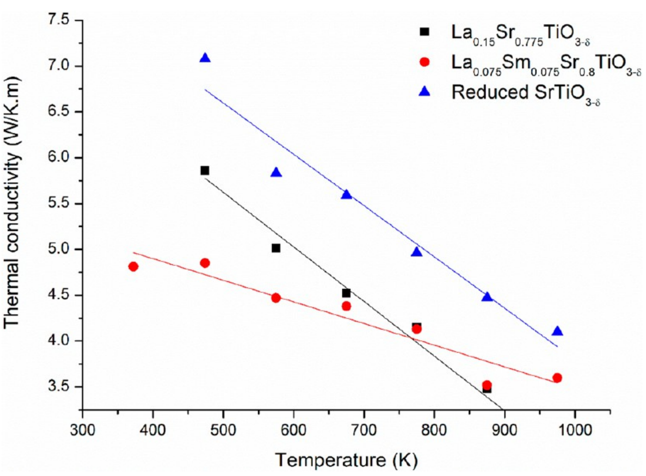

**Figure 13.** Thermal conductivity data for reduced, undoped $SrTiO_3$ and two reduced, A-site RE-doped samples that show a reduction in $\kappa$ at low temperatures. Error bars are not shown here as the data points were generated directly from the laser flash system.

Once relevant values have been extracted from the raw data, $\kappa$ is calculated as shown in Figure 13, which illustrates typical values (with error bars typically between ∼10 to 18%) for reduced, A-site rare earth-doped strontium titanate, as compared to a reduced but undoped sample of $SrTiO_{3-\delta}$. The data illustrate the impact that A-site RE doping has on $\kappa$, especially at lower temperatures.

The thermal conductivity data reported above is obtained directly from the laser flash system while using a standard reference for the estimation of $C_p$ for the sample, as discussed earlier. Overall, it has been reported that using this method can underestimate $\kappa$.[32] As $C_p$ data were not measured, the estimated values can be compared to the Dulong-Petit law, which indicates that $C_p$ should be $3R$ per mole of atoms, where $R$ is the gas constant.[32] The Dulong-Petit limit can be used directly in the calculation of $\kappa$, but it can also be used as a check of measured specific heat data. In their round-robin study, Wang et al.[30,31] showed that measurement of $C_p$, specifically by the DSC method, is the most operator dependent measurement, leading to a 15% scatter in the results of $C_p$ for one material from different laboratories.[31] They were able to dismiss half of the data after determining that it failed the Dulong-Petit test. It is also noteworthy that the actual composition is necessary when determining the Dulong-Petit value.[31] When considering the thermal diffusivity measured from laser flash systems, Wang et al.[31] indicated that scatter up to 17% at 475 K occurred in the data between laboratories, making this measurement as uncertain as direct measurements of $C_p$. The measurement of $\kappa$ can be considered the most significant source of error for the determination of ZT in thermoelectric materials, especially when considering using laser flash systems as it requires the knowledge of the density and specific heat of materials which include their own inherent errors. Other methods for direct measurement and determination of $\kappa$ exist and are covered by Borup et al.[32] and references therein.

### 4.2. Control and Measurement of Electrical Conductivity.

Typical $d^0$ titanate-based perovskite oxides such as $(Ba,Sr,Ca)TiO_3$ are white in appearance and electrically insulating when fired in ambient conditions and require processing under reducing conditions to become blue/black in appearance and electrically semiconducting/metallic. Although a controlled $P(O_2)$ furnace is desirable, it is not essential, and sealed tube furnaces with flowing $N_2/5\%H_2$ are sufficient to reduce such titanates. Reduction occurs through formation of oxygen vacancies ($V_O$) according to eq 9.

$$H_2 + O_O^x \rightarrow V_O^{\bullet\bullet} + 2e' + H_2O \qquad (9)$$

The electrons generated combine with $Ti^{4+}$ ($d^0$) to give $Ti^{3+}$ ($d^1$) ions which give rise to the dramatic change in color and electrical conductivity. The $Ti^{3+}$ ions are reputed to form defect dipoles with $V_O^{\bullet\bullet}$.[16] Much of the literature regarding reduction of electrically insulating $d^0$ containing transition metal oxides to create n-type electrically conducting mixed $d^0$, $d^1$ thermoelectric oxides (eg, titanates, niobates, manganates) indicate a simple setup of flowing 5−10% $H_2$ gas mixtures over a material being fired in a tube furnace.[16,54,55]

To maximize the egress of O from reduced $SrTiO_3$-based materials, it is preferable to have A-site vacancies; i.e., compositions based on the ionic compensation join $Sr_{1-3x/2}RE_xTiO_3$. The perovskite structure may be viewed as an ABC stacking of $AO_3$ layers with 1/4 of the octahedra occupied by $Ti^{4+}$ ions. The O and A ions therefore reside in a pseudo-close packed arrangement in basal planes normal to the stacking direction ($[111]_p$ where p is pseudocubic).[56] The presence of A-site vacancies ($V_A$) therefore encourages diffusion of O and permits a far greater volume of ceramic to be reduced when compared to equivalent RE-doped samples prepared based on electronic compensation, $Sr_{1-x}RE_xTiO_3$. This greater loss of oxygen results in higher $\sigma$ for reduced, A-site deficient $Sr_{1-3x/2}RE_xTiO_{3-\delta}$, and the presence of both $V_A$ and $V_O$ also in principle decreases $\kappa$ by enhancing phonon scattering. This results in higher $ZT$ values for $Sr_{1-3x/2}RE_xTiO_{3-\delta}$ compared to $Sr_{1-x}RETiO_{3-\delta}$ ceramics.[16]

Figure 14 shows $\sigma$ for two ceramics of the same starting composition, one calcined in air and the other in 5% $H_2$ prior to both being sintered in 5% $H_2$. The latter ceramic shows metallic behavior and clearly has substantially higher $\sigma$ at lower temperatures. This may reflect a lower oxygen content in this ceramic;[57] however, the lower $\sigma$ and semiconducting to metallic switch in the former ceramic may reflect the presence of a resistive grain boundary effect associated with incomplete/inhomogeneous removal of oxygen from the reduction process during sintering. Thus, the high temperature $\sigma$ data may be dominated by the grain conductivity, but at lower temperatures resistive grain boundaries suppress the overall conductivity. This could explain the apparent "metal to semiconductor" transition.

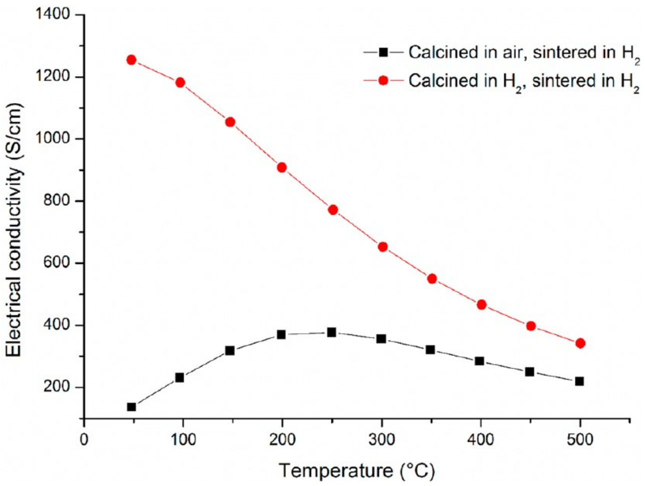

**Figure 14.** $\sigma$ versus temperature (determined by the four-probe method) for samples of $Sm_{0.15}Sr_{0.85}TiO_3$ prepared using different calcination atmospheres (at 1300 °C) but the same sintering atmosphere (1500 °C).

Oxygen partial pressure can be further controlled through the use of water vapor, and as such it is pertinent to mention Ellingham diagrams, which can be found easily in the literature, and give the relative ease of reduction for different metals. These diagrams show the Gibbs free energy ($\Delta G$) vs temperature, which is generally negative due to the decrease in entropy when a gas and a solid react to form another solid.

Four-point probe measurements are the standard method for determining $\sigma$. This method is preferable over simpler methods as it eliminates most additional resistances from, for example, nonohmic electrode contacts associated with a mismatch of work function between the probes and the sample. A survey of additional methods and the uncertainty associated with each can be found in the report by Borup et al.[32]

The setup of a four-probe system is simple: the outer two probes apply a current which creates a voltage across the sample, measured by the two inner probes. These can be used to find the resistance at each point using Ohm's law and then converted into a resistivity, $\rho$, using the dimensions of the sample; $\sigma$ is the reciprocal of this value. This requires that a sample be in specific geometries and have uniform physical properties, e.g., density and thickness. Many commercial instruments have set sample size or probe geometry or require input of the sample dimensions and will do the conversion from resistance to resistivity internally. Hall probe measurements are also beneficial to obtain the carrier concentration directly. With simultaneous $\rho$ measurements, they allow the charge carrier mobility to be determined. Currently, they are not routinely performed in the study of thermoelectrics due to the need for a magnetic field, which is generally less readily available in many academic laboratories. As the range of thermoelectric materials becomes more complex, this technique will become invaluable to the thermoelectrics community, but currently, further discussion here is beyond the scope of this paper.

An example of four-point probe $\sigma$ data is displayed in Figure 15. The data were collected using a Netzsch SBA 458 Nemesis instrument and show a typical trend for two reduced, A-site RE-doped $SrTiO_3$ samples and a reduced (undoped) $SrTiO_3$ for comparison. The samples show a decrease in $\sigma$ with increasing temperature and starkly illustrate the control of $\sigma$ that can be achieved through A-site RE-doping: $\sigma$ at low temperatures is more than an order of magnitude larger than the reduced undoped form, indicating a large increase in the carrier concentration in the sample.

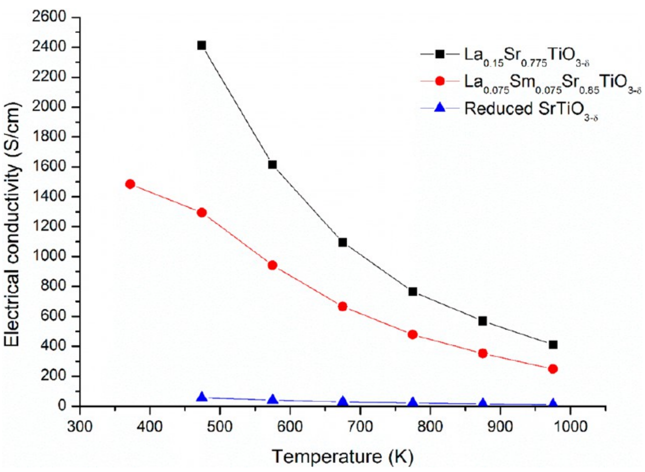

**Figure 15.** $\sigma$ versus temperature for reduced strontium titanate and two A-site doped samples illustrating the effect of increasing the number of charge carriers.

If a commercial instrument is used, the accuracy and reliability of the measurements will be indicated by the manufacturer. In this case, the accuracy is ±5% for electrical conductivity measurements. Each system runs the risk of electrode and thermocouple degradation through aging or reaction with different elements within samples. Checks can be made by running multiple measurement heating and cooling cycles to determine if the data aligns well. If there is any hysteresis or variation in the heating and cooling values determined, either the sample has undergone a change or degraded in the measurement atmosphere or there is a problem with the electrodes or their contact with the sample. Commercial or in-house setups give researchers the opportunity to look at samples in different environments. In the case of reduced perovskite titanates discussed here, Ar is flowing through the system during the measurements. If concerns arise about the material reoxidizing, compressed air or $O_2$ could be used to probe any changes in conductivity of the materials in these working conditions. TGA should also be considered to probe oxidation of samples and if possible retrieve the samples used and perform XRD to investigate any phase degradation or structural changes.

### 4.3. Controlling and Measuring Seebeck Coefficient.

Many commercial instruments are available to measure $S$ and $\sigma$, simultaneously. The benefit of commercial equipment is the ease of use, allowing for the collection of data under constant conditions. Table 2 shows a small selection of these commercial instruments along with their temperature range and other details. While there are differences in each instrument, the operating principles are broadly similar. Again, it is notable that Borup et al.[32] have critically analyzed the measurement of $S$ coefficients wherein they discuss the issues regarding instrument geometries and the thermal and electrical contacts. In the round-robin experiments by Wang et al.,[30] measurement systems, geometries, and errors associated have been analyzed and discussed. To obtain a temperature gradient in some commercial systems, microheaters on either side of the sample are employed. This creates a small temperature difference (up to ~4 K is used for the Netzsch Nemesis; other instruments will have different variations) which induces a voltage across the sample, which can be easily measured. This requires flush contact of the sample to the holder to ensure the transfer of heat to the sample and to measure $S$. The calculation of $S$ is then straightforward, using eq 10.

$$S = \frac{V}{\Delta T} \tag{10}$$

An example of data collected on heating using a Netzsch SBA 458 Nemesis measuring $S$ is shown in Figure 16 for two reduced A-site RE-doped samples of $SrTiO_3$ and a reduced (undoped) $SrTiO_3$. The accuracy of this measurement is ±7%. Here again the influence of carrier concentration can be observed: the magnitude of $S$ in the undoped sample is much greater than that of the doped samples due to its lower $\sigma$, Figure 15, and ultimately has a detrimental effect on $ZT$. In addition to its use in the thermoelectric figure of merit, the Seebeck coefficient may be used to establish if a material is n- or p-type, with a negative value indicating the former, as shown here. With this Netzsch system, the thermocouple geometry is fixed, which addresses concerns posed by Wang et al.[30] about the effect contact location can have on the measured values.

Once reliable $\kappa$, $\sigma$, and S are obtained, $ZT$ can be plotted as a function of temperature. Many authors report an optimum value of $ZT$ at elevated temperatures (>800 °C)[10−16]

**Table 2. Selection of Commercially Available Instruments Used To Measure $S$ and $\sigma$[a]**

| instrument | range of temperatures | atmospheres | range of detectable $\sigma$ or $R$ | notes |
|---|---|---|---|---|
| Netzsch Nemesis SBA 458 | RT−1100 °C | inert, oxidizing, reducing | $0.05-1.5 \times 10^5$ S/cm | fixed thermocouple geometry |
| Linseis LZT-Meter | −150−500 °C or RT−1500 °C | inert, oxidizing, reducing, vacuum | not given | capable of measuring $\kappa$ |
| MMR Technology Seebeck Measurement System | −203−450 °C | air | <100 kΩ | low temperature stage |
| ULVAC ZEM-3 | −80−100 °C or RT−1000 °C | low pressure He | not given | adjustable thermocouple geometry |

[a] The effect of atmosphere on such measurements is discussed elsewhere[58].

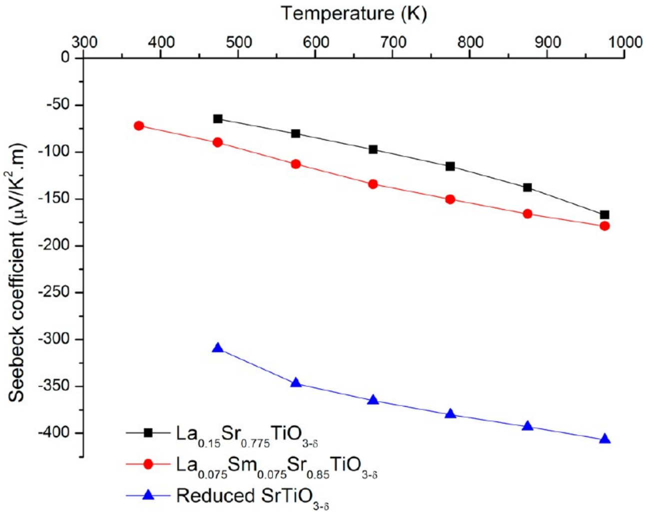

**Figure 16.** *S* versus temperature for reduced (undoped) strontium titanate and two A-site RE-doped samples. The reduction in magnitude of *S* for the RE-doped samples is related to the increase in carrier concentration and $\sigma$ (see Figure 15).

impractical for commercial usage since the construction of the thermoelectric generators (electrodes, connections) are unlikely to withstand extensive usage. The community therefore needs to consider the often less impressive *ZT* values which are obtained at intermediate temperatures (300−700 °C) as these are closer to the values in commercial operation. It has been proposed[59] that $ZT = 0.5$ maybe sufficient for an n-type thermoelectric if the materials is operated at intermediate temperatures and stable to the environment.

Once each of the parameters has been measured, the calculation of *ZT* is straightforward, as given by eq 1. A plot of *ZT* vs temperature for the three materials considered in Figures 13, 15, and 16 is shown in Figure 17. Despite the lower values of *S*, the reduced A-site RE-doped samples show higher *ZT* values than the reduced (undoped) $SrTiO_{3-\delta}$, particularly at intermediate and high temperatures, although these are still lower than some of the best p-type oxide thermoelectrics. The accuracy and percent errors associated with each measurement carry through, leading to a final error in *ZT* of between 14 to 25%.

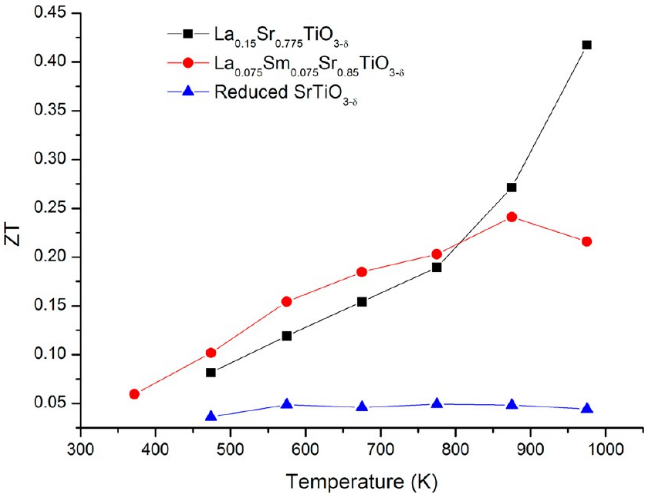

**Figure 17.** Plot of *ZT* vs temperature for two A-site RE-doped and undoped $SrTiO_{3-\delta}$ ceramics.

## 5. GENERAL DISCUSSION

The results presented above illustrate clearly how challenging it is to obtain reliable data on thermoelectric materials which can be compared between laboratories. For accurate and reliable data to be reported, strict adherence to the protocols described is recommended. This is particularly important in the field of thermoelectric oxides in which screening of a large range of oxides is required. There are innumerable candidates for n-type thermoelectric oxides suggested in the literature, including a number of perovskite and perovskite related compounds such as Ruddlesden−Popper phases[60] and tetragonal tungsten bronzes (TTBs).[61−64] In Ruddlesden−Popper compounds the manipulation of the defect chemistry is complicated by the strain criteria imposed by the shear planes in the structure with $V_{Ti}''''$ ionic compensation for A-site La doping proving impossible.[60] Moreover, the rock salt structured shear planes are often highly insulating with limited nonstoichiometry, and thus high levels of $\sigma$ occurs only within the perovskite slabs in 2D, restricting the total value to the point where the PF is no longer high enough to give usable *ZT* despite the improvement in $\kappa$.[60]

TTBs exhibit a wide compositional diversity with the majority based on Nb, Ta, and Ti octahedra.[65] The numerous unfilled sites in the so-called "empty" Ba, RE niobate compounds,[65] ensure high levels of O transport during reduction and have the potential to give rise to high levels of $\sigma$ and therefore optimization of *ZT* in the manner discussed. It is recommended that future work broadens the search for n-type oxides and that TTBs among other systems are screened for *ZT* using the protocols described. However, moving away from classic perovskites with essentially isotropic properties to anisotropic systems such as TTBs may require research into the fabrication of particulates with controlled orientation and morphology so that enhanced thermoelectric properties along specific crystallographic directions can be obtained. Anisotropic crystal structures such RP phases and TTBs generally have particulates with platelet morphology,[66] but the aspect ratios are small and orientation in ceramics is limited. We propose further work is performed on methodologies to create platelet and acicular particle morphologies with higher aspect ratios.

There are numerous novel methods currently in development for the nanoscale control of morphology in thermoelectric and other oxide materials. The prime candidate here is the use of biotemplates to control morphology from the bottom up. Biotemplates are long-chain, naturally occurring molecules which are found in a variety of different sources such as seaweed (sodium alginate)[67] or crab shells (chitin),[68] the mechanisms of which are covered elsewhere.[69]

These templates direct the structure of oxide materials as they form either as replicas of the organic structure or through creation of intermediate inorganic structures which can later lead to interesting or novel morphologies. The types of structures accessible using biotemplates, for example, microspheres,[70] foams,[71] and nanowires,[67] utilizing both direct[70,71] and indirect[67,68,72] means of templating, are shown in Figure 18. These types of methodologies are of particular interest in titanates as the organic biotemplates could be used to locally control $P_{O_2}$ and carbothermally reduce the compound, prior to densification.

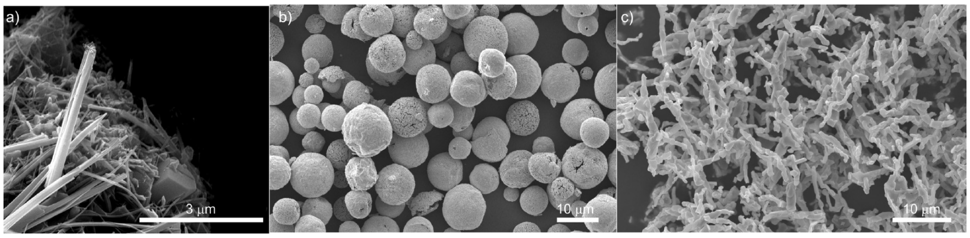

**Figure 18.** SEM micrographs of biotemplated oxides: (a) $BaTiO_3$ nanowires grown using sodium alginate,[67] (b) $YBa_2Cu_3O_7$ hollow microspheres grown using Sephadex gel filtration matrix,[70] and (c) an $YBa_2Cu_3O_7$ foam grown using dextran.[71]

These techniques, although organic in nature, do not suffer from the same issues as hydrothermal techniques in terms of the retention of hydroxyl ions within the structure. As yet, the application of these techniques to thermoelectric oxides is still in the preliminary stages, and it remains to be seen if the nanostructures created can be retained in sintered ceramics and whether any decrease in $\kappa$ is observed. In addition, it is not yet known what effect these morphologies will have on the other physical properties ($\sigma$, $S$), all of which are required for a successful thermoelectric material. Utilizing platelet or acicular particulates with high aspect ratios in screen printing and tape casting (likely routes for scale up to thermoelectric devices) technology results in oriented thick films in which anisotropic properties can be optimized.

## 6. CONCLUSIONS

The protocols for the fabrication and screening of n-type oxides as potential thermoelectrics are described. We strongly urge the community to consider these protocols so that stoichiometry, composition, defect chemistry, and the crystal structure of oxides may be reproduced. Measurement of $\kappa$, $\sigma$, and $S$ are nontrivial with simple procedures described on standard equipment to ensure that accurate and reliable values are determined. We note that many authors report headline values of $ZT$ at elevated temperatures where the use of a commercial device is unlikely. We recommend that comparisons of properties are made at intermediate temperatures (300−700 °C) so that assessment can be made of the true potential of a commercially viable material. Simultaneously, however, there urgently needs to be research into methodologies of encapsulation to prevent reoxidation. Targeting low operating temperatures for reduced oxides minimizes long-term aging through reoxidation but does not eliminate the problem. Consequently, encapsulation in an O impermeable compound is essential. Technologies have existed for encapsulation of NTC thermistors in borosilicate glass to prevent aging, and so in principle this issue is not a "deal breaker". Nonetheless, if reduced oxides become the target of future commercial devices, this issue must be addressed.

For structure determination, the high spatial resolution of electron diffraction and TEM in combination with in-house XRD gives more pertinent insight into phase transitions and local structure (albeit qualitative) than can be obtained through Neutron and Synchroton X-ray sources, and we therefore encourage researchers to explore these techniques when considering reduced ferroic oxides as potential thermoelectrics. For further understanding of the role of O nonstoichiometry and valence within the grains and grain boundaries we propose fine edge structure analysis using electron energy loss spectroscopy (EELS). For the global analysis of cation distributions, mapping using electron probe microanalysis is useful, and energy filtered TEM is an exceptional technique to study the distribution of ions within a grain on the local scale.

Finally, as the screening of oxides moves away from isotropic materials such as perovskites to more anisotropic crystal structures, consideration must be given as to how we optimize $ZT$ of the device through control of orientation.

## ■ AUTHOR INFORMATION

### ORCID

R. Boston: 0000-0002-2131-2236
H. Zhang: 0000-0002-1984-1200
I. M. Reaney: 0000-0003-3893-6544

### Present Address

[†](H.Z.) Materials Science and Engineering Division, National Institute of Standards and Technology, Gaithersburg, Maryland, United States.

### Notes

The authors declare no competing financial interest.

## ■ ACKNOWLEDGMENTS

We acknowledge the EPSRC for financial support of the Substitution and Sustainability of Functional Materials and Devices EPSRC grant (EP/L017563/1) and a DTA studentship (G.D.L.). A.C.I. thanks TETFUND, Nigeria, for financial support.

## ■ REFERENCES

(1) US Department of Energy. *Quadrennial Technology Review 2015*; 2015.

(2) US Department of Energy. *Quadrennial Technology Review 2015*; 2015; Chapter 6.

(3) http://www.eia.gov/tools/faqs/faq.cfm?id=104&t=3 (accessed Oct. 19, 2016).

(4) Fergus, J. W. Oxide Materials for High Temperature Thermoelectric Energy Conversion. *J. Eur. Ceram. Soc.* **2012**, *32*, 525−540.

(5) Twaha, S.; Zhu, J.; Yan, Y.; Li, B. A Comprehensive Review of Thermoelectric Technology: Materials, Applications, Modelling and Performance Improvement. *Renewable Sustainable Energy Rev.* **2016**, *65*, 698−726.

(6) Zou, H.; Rowe, D. M.; Min, G. Growth of p- and n-type Bismuth Telluride Thin Films by Co-evaporation. *J. Cryst. Growth* **2001**, *222*, 82−87.

(7) Riffat, S. B.; Ma, X. Thermoelectrics: A Review of Present and Potential Applications. *Appl. Therm. Eng.* **2003**, *23*, 913−935.

(8) Poudel, B.; Hao, Q.; Ma, Y.; Lan, Y.; Minnich, A.; Yu, B.; Yan, X.; Wang, D.; Muto, A.; Vashaee, D.; Chen, X.; Liu, J.; Dresselhaus, M. S.; Chen, G.; Ren, Z. High-Thermoelectric Performance of Nanostructured Bismuth Antimony Telluride Bulk Alloys. *Science* **2008**, *320*, 634−638.

(9) Ohtaki, M.; Koga, H.; Tokunaga, T.; Eguchi, K.; Arai, H. Electrical Transport Properties and High-Temperature Thermoelectric Performance of $(Ca_{0.9}M_{0.1})MnO_3$ (M = Y, La, Ce, Sm, In, Sn, Sb, Pb, Bi). *J. Solid State Chem.* **1995**, *120*, 105−111.

(10) Krasutskaya, N. S.; Klyndyuk, A. I.; Evseeva, L. E.; Tanaeva, S. A. Synthesis and Properties of $Na_xCoO_2$ (x = 0.55, 0.89) Oxide Thermoelectrics. *Inorg. Mater.* **2016**, *52*, 393−399.

(11) Wang, Y.; Sui, Y.; Wang, X.; Su, W.; Liu, X. Enhanced High Temperature Thermoelectric Characteristics of Transition Materials Doped $Ca_3Co_4O_{9-\delta}$ by Cold High Pressure Fabrication. *J. Appl. Phys.* **2010**, *107*, 033708.

(12) Zhang, F. P.; Lu, Q. M.; Zhang, J. X. Synthesis and High Temperature Thermoelectric Properties of $Ba_xAg_yCa_{3-x-y}Co_4O_9$ Compounds. *J. Alloys Compd.* **2009**, *484*, 550−554.

(13) Kikuchi, A.; Okinaka, N.; Akiyama, T. A Large Thermoelectric Figure of Merit of La-Doped $SrTiO_3$ Prepared by Combustion Synthesis with Post-Spark Plasma Sintering. *Scr. Mater.* **2010**, *63*, 407−410.

(14) Wang, H. C.; Wang, C. L.; Su, W. B.; Liu, J.; Zhao, Y.; Peng, H.; Zhang, J. L.; Zhao, M. L.; Li, J. C.; Yin, N.; Mei, L. M. Enhancement of Thermoelectric Figure of Merit by Doping Dy in $La_{0.1}Sr_{0.9}TiO_3$ Ceramic. *Mater. Res. Bull.* **2010**, *45*, 809−812.

(15) Wang, Y.; Sui, Y.; Su, W.; Wang, X. Enhancement of Thermoelectric Efficiency in (Ca, Dy)$MnO_3$-(Ca, Yb)$MnO_3$ Solid Solutions. *Appl. Phys. Lett.* **2010**, *97*, 052109.

(16) Lu, Z.; Zhang, H.; Lei, W.; Sinclair, D. C.; Reaney, I. M. High-Figure-of-Merit Thermoelectric La-Doped A-Site-Deficient $SrTiO_3$ Ceramics. *Chem. Mater.* **2016**, *28*, 925−935.

(17) Gaultois, M. W.; Sparks, T. D.; Borg, C. K. H.; Seshadri, R.; Bonificio, W. D.; Clarke, D. R. Data-Driven Review of Thermoelectric Materials: Performance and Resource Considerations. *Chem. Mater.* **2013**, *25*, 2911−2920.

(18) Chen, G. Phonon Heat Conduction in Nanostructures. *Int. J. Therm. Sci.* **2000**, *39*, 471−480.

(19) Li, M.; Zhang, H.; Cook, S. N.; Li, L.; Kilner, J. A.; Reaney, I. M.; Sinclair, D. C. Dramatic Influence of A-site Nonstoichiometry on the Electrical Conductivity and Conduction Mechanisms in the Perovskite Oxide $Na_{0.5}Bi_{0.5}TiO_3$. *Chem. Mater.* **2015**, *27*, 629−634.

(20) Akin, I.; Li, M.; Lu, Z.; Sinclair, D. C. Oxygen-loss in A-site deficient $Sr_{0.85}La_{0.10}TiO_3$ perovskite. *RSC Adv.* **2014**, *4*, 32549−32554.

(21) Chang, C.-Y.; Wang, W.-N.; Huang, C.-Y. The Effect of MgO and Rare-Earth Oxide on Formation Behavior of Core-Shell Structure in $BaTiO_3$. *J. Am. Ceram. Soc.* **2013**, *96*, 2570−2576.

(22) Bäurer, M.; Kungl, H.; Hoffmann, M. J. Influence of Sr/Ti Stoichiometry on the Densification Behaviour of Strontium Titanate. *J. Am. Ceram. Soc.* **2009**, *92*, 601−606.

(23) Sallé, C.; Maître, A.; Baumard, J.-F.; Rabinovitch, Y. A First Approach of Silica Effect on the Sintering of Nd:YAG. *Opt. Rev.* **2007**, *14*, 169−172.

(24) Glinchuk, M. D.; Bykov, I. P.; Kornienko, S. M.; Laguta, V. V.; Slipenyuk, A. M.; Bilous, A. G.; V'yunov, O. I.; Yanchevskii, O. Z. Influence of Impurities on the Properties of Rare-Earth-Doped Barium-Titanate Ceramics. *J. Mater. Chem.* **2000**, *10*, 941−947.

(25) Balakrishna, P.; Chakraborthy, K. P.; Singh, A. End-capping and other defects in pressed ceramic compacts. *Indian J. Eng. Mater. Sci.* **1996**, *3*, 196−200.

(26) Fischer, G. J.; Wang, Z.; Karato, S. Elasticity of $CaTiO_3$, $SrTiO_3$ and $BaTiO_3$ perovskite up to 3.0 GPa: the effect of crystallographic structure. *Phys. Chem. Miner.* **1993**, *20*, 97−103.

(27) Guo, J.; Guo, H.; Baker, A. L.; Lanagan, M. T.; Kupp, E. R.; Messing, G. L.; Randall, C. A. Cold sintering: a paradigm shift for processing and integration of ceramics. *Angew. Chem., Int. Ed.* **2016**, *55*, 11457−11461.

(28) Glazer, A. M. Simple Ways of Determining Perovskite Structures. *Acta Crystallogr., Sect. A: Cryst. Phys., Diffr., Theor. Gen. Crystallogr.* **1975**, *31*, 756−762.

(29) Snyder, G. J.; Toberer, E. S. Complex Thermoelectric Materials. *Nat. Mater.* **2008**, *7*, 105−114.

(30) Wang, H.; Porter, W. D.; Böttner, H.; König, J.; Chen, L.; Bai, S.; Tritt, T. M.; Mayolet, A.; Senawiratne, J.; Smith, C.; Harris, F.; Gilbert, P.; Sharp, J. W.; Lo, J.; Kleinke, H.; Kiss, L. Transport Properties of Bulk Thermoelectrics—An International Round-Robin Study, Part I: Seebeck Coefficient and Electrical Resistivity. *J. Electron. Mater.* **2013**, *42*, 654−664.

(31) Wang, H.; Porter, W. D.; Böttner, H.; König, J.; Chen, L.; Bai, S.; Tritt, T. M.; Mayolet, A.; Senawiratne, J.; Smith, C.; Harris, F.; Gilbert, P.; Sharp, J. W.; Lo, J.; Kleinke, H.; Kiss, L. Transport Properties of Bulk Thermoelectrics—An International Round-Robin Study, Part II: Thermal Diffusivity, Specific Heat, and Thermal Conductivity. *J. Electron. Mater.* **2013**, *42*, 1073−1084.

(32) Borup, K. A.; de Boor, J.; Wang, H.; Drymiotis, F.; Gascoin, F.; Shi, X.; Chen, L.; Fedorov, M. I.; Müller, E.; Iversen, B. B.; Snyder, G. J. Measuring Thermoelectric Transport Properties of Materials. *Energy Environ. Sci.* **2015**, *8*, 423−435.

(33) Winter, M. R.; Clarke, D. R. Oxide Materials with Low Thermal Conductivity. *J. Am. Ceram. Soc.* **2007**, *90*, 533−540.

(34) Koumoto, K.; Wang, Y.; Zhang, R.; Kosuga, A.; Funahashi, R. Oxide Thermoelectric Materials: A Nanostructuring Approach. *Annu. Rev. Mater. Res.* **2010**, *40*, 363−394.

(35) Buscaglia, M. T.; Maglia, F.; Anselmi-Tamburini, U.; Marre, D.; Pallecchi, I.; Ianculescu, A.; Canu, G.; Viviani, M.; Fabrizio, M.; Buscaglia, V. Effect of Nanostructure on the Thermal Conductivity of La-Doped $SrTiO_3$ Ceramics. *J. Eur. Ceram. Soc.* **2014**, *34*, 307−316.

(36) Wang, H.; Su, W.; Liu, J.; Wang, C. Recent Development of n-type Perovskite Thermoelectrics. *J. Materiomics* **2016**, *2*, 225−236.

(37) He, J.; Liu, Y.; Funahashi, R. Oxide Thermoelectrics: The Challenges, Progress and Outlook. *J. Mater. Res.* **2011**, *26*, 1762−1772.

(38) Pei, J.; Chen, G.; Zhou, N. Hydrothermal Synthesis, Characterization, Electronic Structure, and Thermoelectric Properties of $(Ca_{0.85}OH)_{1.16}CoO_2$. *J. Chem. Phys.* **2009**, *130*, 044706.

(39) Culebras, M.; Torán, R.; Gómez, C. M.; Cantarero, A. $La_{1-x}Ca_xMnO_3$ Semiconducting Nanostructures: Morphology and Thermoelectric Properties. *Nanoscale Res. Lett.* **2014**, *9*, 415.

(40) Shao, Y.; Sun, J.; Gao, L. Hydrothermal Synthesis of Hierarchical Nanocolumns of Cobalt Hydroxide and Cobalt Oxide. *J. Phys. Chem. C* **2009**, *113*, 6566−6572.

(41) Hicks, L. D.; Dresselhaus, M. S. Effect of Quantum-Well Structures on the Thermoelectric Figure of Merit. *Phys. Rev. B: Condens. Matter Mater. Phys.* **1993**, *47*, 12727−12731.

(42) Xu, G.; Huang, X.; Zhang, Y.; Deng, S.; Wei, X.; Shen, G.; Han, G. Self-Assembly and Formation Mechanism of Single-Crystal $SrTiO_3$ Nanosheets via Solvothermal Route with Ethylene Glycol as Reaction Medium. *CrystEngComm* **2013**, *15*, 7206−7211.

(43) Kuang, Q.; Yang, S. Template Synthesis of Single-Crystal-Like Porous $SrTiO_3$ Nanocube Assemblies and Their Enhanced Photocatalytic Hydrogen Evolution. *ACS Appl. Mater. Interfaces* **2013**, *5*, 3683−3690.

(44) da Silva, L. F.; Avansi, W.; Andrés, J.; Ribeiro, C.; Moreira, M. L.; Longo, E.; Mastelaro, V. R. Long-Range and Short-Range Structures of Cube-Like Shape $SrTiO_3$ Powders: Microwave-Assisted Hydrothermal Synthesis and Photocatalytic Activity. *Phys. Chem. Chem. Phys.* **2013**, *15*, 12386−12393.

(45) Liu, Y.; Lin, Y.; Shi, Z.; Nan, C.-W.; Shen, Z. Preparation of $Ca_3Co_4O_9$ and improvement of its Thermoelectric Properties by Spark Plasma Sintering. *J. Am. Ceram. Soc.* **2005**, *88*, 1337−1340.

(46) Kim, K. H.; Shim, S. H.; Shim, K. B.; Niihara, K.; Hojo, J. Microstructural and Thermoelectric Characteristics of Zinc Oxide-Based Thermoelectric Materials Fabricated using a Spark Plasma Sintering Process. *J. Am. Ceram. Soc.* **2005**, *88*, 628−632.

(47) (a) *Standard Test Method for Thermal Diffusivity by the Flash Method*; ASTM E1461-13; ASTM International: West Conshohocken, PA, 2013; DOI: https://doi.org/10.1520/E1461. (b) *Standard Practice for Thermal Diffusivity by the Flash Method*; ASTM E2585-09; ASTM International: West Conshohocken, PA, 2015; DOI: https://doi.org/10.1520/E2585-09R15.

(48) Leitner, J.; Chuchvalec, P.; Sedmidubský, D.; Strejc, A.; Abrman, P. Estimation of Heat Capacities of Solid Mixed Oxides. *Thermochim. Acta* **2002**, *395*, 27−46.

(49) Leitner, J.; Voňka, P.; Sedmidubský, D.; Svoboda, P. Application of Neumann−Kopp Rule for the Estimation of Heat Capacity of Mixed Oxides. *Thermochim. Acta* **2010**, *497*, 7−13.

(50) Parker, W. L.; Jenkins, R. J.; Butler, C. P.; Abbott, G. L. Flash Method of Determining Thermal Diffusivity, Heat Capacity, and Thermal Conductivity. *J. Appl. Phys.* **1961**, *32*, 1679−1684.

(51) Cowan, R. D. Pulse Method of Measuring Thermal Diffusivity at High Temperatures. *J. Appl. Phys.* **1963**, *34*, 926−927.

(52) Heckman, R. C. Finite Pulse-Time and Heat-Loss Effects in Pulse Thermal Diffusivity Measurements. *J. Appl. Phys.* **1973**, *44*, 1455−1460.

(53) Clark, L. M., III; Taylor, R. E. Radiation Loss in the Flash Method for Thermal Diffusivity. *J. Appl. Phys.* **1975**, *46*, 714−719.

(54) Kovalevsky, A. V.; Yaremchenko, A. A.; Populoh, S.; Thiel, P.; Fagg, D. P.; Weidenkaff, A.; Frade, J. R. Towards a High Thermoelectric Performance in Rare-Earth Substituted SrTiO$_3$: Effects Provided by Strongly-Reducing Sintering Conditions. *Phys. Chem. Chem. Phys.* **2014**, *16*, 26946−26954.

(55) Wang, H. C.; Wang, C. L.; Su, W. B.; Liu, J.; Sun, Y.; Peng, H.; Mei, L. M. doping Effect of La and Dy on the Thermoelectric Properties of SrTiO$_3$. *J. Am. Ceram. Soc.* **2011**, *94*, 838−842.

(56) West, A. R. *Solid State Chemistry and its Applications*; Wiley and Sons: 2014.

(57) Lee, C.; Yahia, J.; Brebner, J. L. Electronic Conduction in Slightly Reduced Strontium Titanate at Low Temperatures. *Phys. Rev. B* **1971**, *3*, 2525−2533.

(58) Gajović, A.; Šantić, A.; Djerdj, I.; Tomašić, N.; Moguš-Milanković, A.; Su, D. S. Structure and Electrical Conductivity of Porous Zirconium Titanate Ceramics Produced by Mechanochemical Treatment and Sintering. *J. Alloys Compd.* **2009**, *479*, 525−531.

(59) Private communication with K. Simpson of European Thermodynamics.

(60) Lu, Z.; Sinclair, D. C.; Reaney, I. M. The Influence of La Doping and Heterogeneity on the Thermoelectric Properties of Sr$_3$Ti$_2$O$_7$ Ceramics. *J. Am. Ceram. Soc.* **2016**, *99*, 515−522.

(61) Bock, J. A.; Trolier-McKinstry, S.; Mahan, G. D.; Randall, C. A. Polarization-Based Perturbations to Thermopower and Electronic Conductivity in Highly Conductive Tungsten Bronze Ttructured (Sr, Ba) Nb$_2$O$_6$: Relaxors vs Normal Ferroelectrics. *Phys. Rev. B: Condens. Matter Mater. Phys.* **2014**, *90*, 115106.

(62) Kieslich, G.; Birkel, C. S.; Douglas, J. E.; Gaultois, M.; Veremchuk, I.; Seshadri, R.; Stucky, G. D.; Grin, Y.; Tremel, J. SPS-Assisted Preparation of the Magneli Phase WO$_{2.90}$ for Thermoelectric Applications. *J. Mater. Chem. A* **2013**, *1*, 13050−13054.

(63) Gaultois, M. W.; Douglas, J. E.; Sparks, T. D.; Seshadri, R. Single-Step Preparation and Consolidation of Reduced Early-Transition-Metal Oxide/Metal n-type Thermoelectric Composites. *AIP Adv.* **2015**, *5*, 097144.

(64) Stennett, M. C.; Reaney, I. M.; Miles, G. C.; Woodward, D. I.; West, A. R.; Kirk, C. A.; Levin, I. Dielectric and Structural Studies of Ba$_2$MTi$_2$Nb$_3$O$_{15}$ (BMTNO15, M= Bi$^{3+}$, La$^{3+}$, Nd$^{3+}$, Sm$^{3+}$, Gd$_{3+}$) Tetragonal Tungsten Bronze-Structured Ceramics. *J. Appl. Phys.* **2007**, *101*, 104114.

(65) Zhu, X.; Fu, M.; Stennett, M. C.; Vilarinho, P. M.; Levin, I.; Randall, C. A.; Gardner, J.; Morrison, F. D.; Reaney, I. M. A Crystal-Chemical Framework for Relaxor Versus Normal Ferroelectric Behaviour in Tetragonal Tungsten Bronzes. *Chem. Mater.* **2015**, *27*, 3250−3261.

(66) Lee, S.; Wilke, H. T.; Trolier-McKinstry, S.; Zhang, S.; Randall, C. A. Sr$_x$Ba$_{1-x}$Nb$_2$O$_{6-\delta}$ Ferroelectric-thermoelectrics: Crystal Anisotropy, Conduction Mechanism, and Power Factor. *Appl. Phys. Lett.* **2010**, *96*, 031910.

(67) Schnepp, Z.; Wimbush, S. C.; Mann, S.; Hall, S. R. Alginate-Mediated Routes to the Selective Synthesis of Complex Metal Oxide Nanostructures. *CrystEngComm* **2010**, *12*, 1410−1415.

(68) Hall, S. R. Biomimetic Synthesis of High-T$_c$, Type-II Superconductor Nanowires. *Adv. Mater.* **2006**, *18*, 487−490.

(69) Schnepp, Z. Biopolymers as a Flexible Resource for Nanochemistry. *Angew. Chem., Int. Ed.* **2013**, *52*, 1096−108.

(70) Boston, R.; Carrington, A.; Walsh, D.; Hall, S. R. Synthesis of Spherical Superconductors. *CrystEngComm* **2013**, *15*, 3763−3766.

(71) Walsh, D.; Wimbush, S. C.; Hall, S. R. Use of the Polysaccharide Dextran as a Morphological Directing Agent in the Synthesis of High-T$_c$ Superconducting YBa$_2$Cu$_3$O$_{7-\delta}$ Sponges with Improved Critical Current Densities. *Chem. Mater.* **2007**, *19*, 647−649.

(72) Schnepp, Z. A. C.; Wimbush, S. C.; Mann, S.; Hall, S. R. Structural Evolution of Superconductor Nanowires in Biopolymer Gels. *Adv. Mater.* **2008**, *20*, 1782−1786.